mathematics

MDPI

Article

Design Optimization of 3-DOF Redundant Planar Parallel Kinematic Mechanism Based Finishing Cut Stage for Improving Surface Roughness of FDM 3D Printed Sculptures

Minbok Lee [1], Hyungjin Jeong [2] and Donghun Lee [2,*]

[1] Mechanism Research Department, Hyundai Robotics, Seongnam 13615, Korea; minbok.lee10@gmail.com
[2] School of Mechanical Engineering, Soongsil University, Seoul 06978, Korea; hyungjin.jeong2@gmail.com
* Correspondence: dhlee04@ssu.ac.kr; Tel.: +82-2-828-7020

Abstract: This paper describes the optimal design of a 3-DOF redundant planar parallel kinematic mechanism (PKM) based finishing cut stage to improve the surface roughness of FDM 3D printed sculptures. First, to obtain task-optimized and singularity minimum workspace of the redundant PKM, a weighted grid map based design optimization was applied for a task-optimized workspace without considering the redundancy. For the singularity minimum workspace, the isotropy and manipulability of the end effector of the PKM were carefully modeled under the previously obtained redundancy for optimality. It was confirmed that the workspace size increased by 81.4%, and the internal singularity significantly decreased. To estimate the maximum rated torque and torsional stiffness of all active joints and prevent an undesired end effector displacement of more than 200 μm, a kinematic stiffness model composed of active and passive kinematic stiffness was derived from the virtual work theorem, and the displacement characteristic at the end effector was examined by applying the reaction force for the PLA surface finishing as an external force acting at the end effector. It was confirmed that the displacement of the end effector of a 1-DOF redundant PKM was not only less than 200 μm but also decreased from 40.9% to 67.4% compared to a nonredundant actuation.

Keywords: hybrid 3D printer; finishing cut stage; parallel kinematic mechanism; workspace optimization; surface roughness

Citation: Lee, M.; Jeong, H.; Lee, D. Design Optimization of 3-DOF Redundant Planar Parallel Kinematic Mechanism Based Finishing Cut Stage for Improving Surface Roughness of FDM 3D Printed Sculptures. *Mathematics* **2021**, *9*, 961. https://doi.org/10.3390/math9090961

Academic Editor: Carlos Llopis-Albert

Received: 27 March 2021
Accepted: 21 April 2021
Published: 25 April 2021

1. Introduction

To meet the demand in various fields, the global 3D printer market has grown by more than 15% annually since 2014. In addition, 3D printers are typically classified into fused deposition modeling (FDM), a stereolithography apparatus (SLA), and selective laser sintering (SLS) according to the production method of the sculpture. Among them, the FDM method, which is a method for laminating industrial plastics such as PLA and ABS by heating at high temperatures, has a market share of more than 20% in the global market owing to its low cost and simple lamination technology. However, the FDM method has a slow molding speed and low surface roughness of the sculpture owing to the characteristics of the additive manufacturing method in which materials are stacked one by one through high heat nozzles; it is therefore necessary to develop a technology to compensate for this [1,2].

Figure 1 shows a complex 3D printer commercially available around the world. Figure 1a shows a Lasertec 65 3D printer of DMG-MORI, Germany, which improves the surface roughness of metal sculptures by combining the laser metal deposition (LMD) method of melting metal materials with a high-energy source to make sculptures with a mechanical cutting method through an existing 5-axis cutting machine. Figure 1b shows a LUMEX Avance-25 of Matsuura, Japan, which improves the surface roughness of metal sculptures by combining the SLS method, which combines the materials by irradiating a high-energy beam on the metal materials, with the mechanical cutting method. Figure 1c

shows Stratasys' smoothing station in the United States, which can improve the surface roughness of 3D-printed sculptures through chemical processing. However, the Lasertec 65 3D and LUMEX Avance-25 were developed for metal molding and cutting, and thus the strength and stiffness of the cutting mechanism are high, the installation area is wide (i.e., 12 m^2 each), and the selling price is high. In addition, in the case of the smoothing station, because the post-process is performed through a chemical process, unintended rounding occurs in the sculpture, and additional workspace and time are required for the post-process. In other words, the technology required for improving the surface roughness of a commercialized complex 3D printer is unsuitable for improving the surface roughness of FDM-type sculptures. Therefore, to improve the surface roughness performance of the FDM lamination method, it is necessary to design a mechanical finishing cut stage optimized for industrial plastic processing.

Figure 1. Commercialized 3D printer with surface quality improvement function: (**a**) Lasertec 65 3D, (**b**) LUMEX Avance-25, and (**c**) smoothing station.

The parallel kinematic mechanism (PKM) is mainly used for the cutting stage rather than the serial kinematic mechanism (SKM) [3–6]. This is because the PKM, which is generally composed of a fixed platform and several links, has a higher stiffness than the SKM and is suitable for the cutting stage, where the stiffness characteristics of the tool are important. However, owing to this structure, the PKM has a high dependence on kinematic parameters, and thus many constraint conditions limiting the range of motion at the tool tip exist in the PKM, and it does not have a wide workspace [7–13]. Therefore, a hybrid mechanism that combines the SKM and the PKM has been researched and developed in a field where a wide workspace compared to the size of the mechanism and high stiffness is required [14–20]. However, because of the characteristics of the hybrid structure in which the PKM and SKM are connected in series, issues regarding the area, shape, and singularity of the workspace of the PKM are still inherent. Because these two issues affect the performance of the hybrid mechanism independently of each other, an optimal design that considers both should be carried out [21–26]. Huang et al. [27] defined the average Jacobian condition number for a rectangular-shaped area in the workspace as a GCI and the ratio of the area of a rectangular-shaped workspace to the maximum area as an evaluation index for that workspace. In addition, a kinematic parameter optimization was applied by maximizing the ratio of the GCI to the evaluation index of the workspace of the symmetrical 2-DOF 5R PKM. Lara Molinar et al. [28] applied a GCI and a GGI, which are operability evaluation indices, and a GPI, which is a force transmission rate evaluation index, as objective functions within a cuboid-shaped workspace for the optimal design of the 6-DOF Gough–Stewart PKM and conducted a multipurpose optimization. Huang and Thebert [29] presented an evaluation index called the overall dexterity, including the workspace and singularity, and optimized kinematic parameters for the optimal design of the RRR type and RPR type 3-DOF PKM. Huang et al. [30] experimentally examined the

ratio between kinematic parameters (dimensional synthesis) to obtain the optimum shape that improves the operating performance while securing the cylindrical workspace of the TriVariant, a 3-DOF PKM. Laribi [31] optimized the kinematic parameters such that the GCI in the workspace was maximized while securing the required work area of a semispherical shape of 3-DOF SPM-PKM. As such, many studies have been conducted to simultaneously solve the problem of workspace and singularity of the PKM, which can also solve the problem of the PKM inherent in the hybrid mechanism.

In this paper, a new 3-DOF planar hybrid finishing cut stage that expands the workspace by combining a 2-DOF PKM at the end effector of a constrained 1-DOF rotary motion is presented, and an optimization method to simultaneously improve the work area efficiency and singularity characteristics is presented. In Section 2, a kinematic analysis applied to the workspace and a singularity analysis of the proposed mechanism are described, and in Section 3, an optimization of the kinematic design parameters and singularity analysis conducted to expand the workspace area are detailed. In Section 4, a mechanical stiffness model is established based on the virtual work theory, and the end effector displacement characteristics of the PLA materials are reviewed when considering the cutting reaction force.

2. Kinematic Analysis of Hybrid "Serial–Parallel" 3-DOF Parallel Kinematic Mechanism

2.1. Structure of 3-DOF Planar PKM

As shown in Figure 2, the proposed mechanism is a structure in which a gosselin-based 2-DOF planar parallel mechanism with an arc-shaped frame as the base frame is connected to a circular guide. The arc-shaped frame rotates about the z-axis at the center of the circular guide, and at the same time, the planar PKM rotates along the frame. The 2-DOF planar PKM is a structure in which two 2-bar serial chains and one 1-bar serial chain are connected to a triangular platform, unlike the existing gosselin 3-RRR planar PKM. To drive this, nine rotation joints are needed: one rotation joint q_1 is fixed to {B}, which is the center of the circular guide, and the other eight rotation joints are composed of three rotation joints $B_i(i = 1,\ 2,\ 3)$ in an arc-shaped frame, two rotation joints $S_i(i = 1,\ 2)$ connecting B and the 2-bar serial chain, and three rotation joints $P_i(i = 1,\ 2,\ 3)$ located at the vertices of the triangular platform.

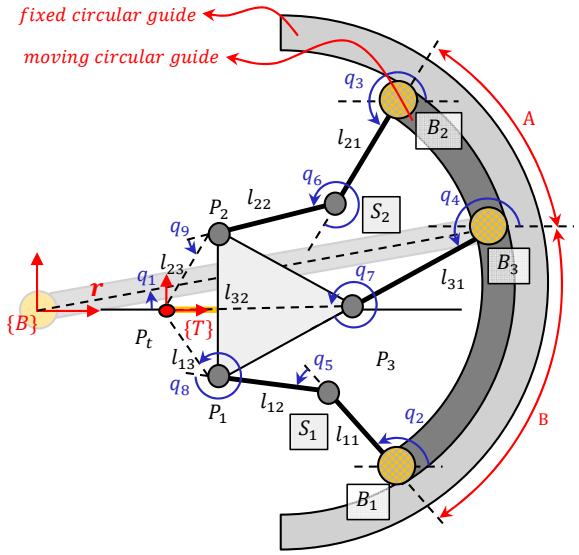

Figure 2. Kinematic model of 3-DOF planar parallel kinematic mechanism.

2.2. Kinematic Analysis

To analyze the workspace and singularity properties of the planar PKM, the relationship between the joint value and the posture of the end effector must be determined, which can be achieved through a kinematic analysis.

2.2.1. Inverse Kinematic

The purpose of the inverse kinematic analysis is to express the value of each joint in an analytic form, given the position and orientation of the end effector. It is calculated using the constraint conditions of the planar PKM structure.

First, as shown in Figure 3, a rotation matrix R representing the relationship between the posture of the tool frame {T} and the posture of the base frame {B}, which changes according to the posture at the end effector, is calculated. Because the proposed mechanism is a planar mechanism, the rotation matrix R rotates only along the z-axis.

$$R = \begin{bmatrix} \cos(\theta) & -\sin(\theta) \\ \sin(\theta) & \cos(\theta) \end{bmatrix} \tag{1}$$

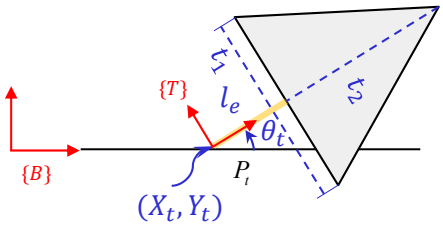

Figure 3. Position and orientation of tool frame and information of the designed triangle platform.

To calculate the position of joint ${}^{T}P_i (i = 1,\ 2,\ 3)$ on the triangular platform with respect to {T}, the height (t_2) and length (t_1) of the triangular platform and the length (l_e) of the end-mill are used.

$${}^{T}P_i = \begin{bmatrix} l_e \\ -(1/2)t_1 \end{bmatrix},\ {}^{T}P_2 = \begin{bmatrix} l_e \\ (1/2)t_1 \end{bmatrix},\ {}^{T}P_3 = \begin{bmatrix} l_e + t_2 \\ 0 \end{bmatrix} \tag{2}$$

Using the rotation matrix R of (1), the position of the joint ${}^{T}P_i (i = 1,\ 2,\ 3)$ on the triangular platform with respect to {T} can be expressed as ${}^{B}P_i (i = 1, 2, 3)$ w.r.t. {B}.

$${}^{T}P_i = \begin{bmatrix} x_t \\ y_t \end{bmatrix} + R\left({}^{T}P_i\right), (i = 1, 2, 3) \tag{3}$$

The rotation angle (q_1) of the arc-shaped frame at the center of the circular slide, the value $(q_2,\ q_3, q_4)$ of the rotational joint $B_i (i = 1,\ 2,\ 3)$ on the arc-shaped frame, the value $(q_5,\ q_6)$ of the joint $S_i (i = 1,\ 2)$ connecting the 2-bar serial chain, and the value $(q_7,\ q_8, q_9)$ of the joint $P_i (i = 1,\ 2,\ 3)$ on the triangular platform can be calculated. First, q_1 is calculated using the constraint condition based on the difference between the position vector of the B_3 joint with respect to {B} with the size of the circular guide radius r and the position vector of P_3, also with respect to {B}.

$$L_{31} = \|P_3 - B_3\| \tag{4}$$

Equation (4) is decomposed using the x, y components and is summarized as shown in Equation (5) below.

$$(P_{3_x} - B_{3_x})^2 + \left(P_{3_y} - B_{3_y}\right)^2 - l_{31}^2 = 0 \tag{5}$$

In Equation (5), the vector of B_3 is expressed as $B_{3,x} = r\ cos(q_1), B_{3,y} = r\ sin(q_1)$, through the rotational radius of the circular guide r and joint value q_1 by substituting

$\sin(q_1) = \frac{2T}{1+T^2}$, $\cos(q_1) = \frac{1-T^2}{1+T^2}$ and can be expressed as a quadratic equation for T. Among the two solutions of the quadratic equation, q1 is selected as the one that minimizes the distance between P_2 and B_3.

$$q_1 = arctan2\left(\frac{2T}{1+T}, \frac{1-T^2}{1+T^2}\right) \tag{6}$$

Knowing the value of q_1, the position of $B_i (I = 1,\ 2,\ 3)$ can be calculated using Equation (7).

$$B_1 = \begin{bmatrix} r\cos(q_1+B) \\ r\sin(q_1+B) \end{bmatrix}, B_2 = \begin{bmatrix} r\cos(q_1+A) \\ r\sin(q_1+A) \end{bmatrix}, B_3 = \begin{bmatrix} r\cos(q_1) \\ r\sin(q_1) \end{bmatrix} \tag{7}$$

Using Equations (7) and (8), which give a constraint in which the distance between joint S_i and P_i is l_{i2}, q_2 and q_3 can be calculated as in Equation (9). The calculation process uses a substitution similar to the process when calculating q_1.

$$L_{i2} = \|S_i - P_i\| \ \ (i = 1, 2) \tag{8}$$

$$q_{i+1} = arctan2\left(\frac{2T}{1+T}, \frac{1-T^2}{1+T^2}\right) \tag{9}$$

Using the previously calculated q_1, q_2, q_3 and the kinematics of each serial chain, the values of the remaining six joints can be calculated.

$$q_4 = \arctan2\left(\frac{(y)_{P_3} - (y)_{B_3}}{L_{31}}, \frac{(x)_{P_3} - (x)_{B_3}}{L_{31}}\right) \tag{10}$$

$$q_{i+4} = \arctan2\left(\frac{(y)_{P_i} - L_{i1}\sin(q_{i+1}) - (y)_{B_i}}{L_{i2}}, \frac{(x)_{P_i} - L_{i1}\cos(q_{i+1}) - (x)_{B_i}}{L_{i2}}\right) - q_{i+1} (i = 1,\ 2) \tag{11}$$

$$q_7 = \arctan2\left(\frac{(y)_{P_t} - (y)_{P_3}}{L_{32}}, \frac{(x)_{P_t} - (x)_{P_3}}{L_{32}}\right) - q_4 \tag{12}$$

$$q_{i+7} = \arctan2\left(\frac{(y)_{P_t} - (y)_{P_j}}{L_{j3}}, \frac{(x)_{P_t} - (x)_{P_j}}{L_{j3}}\right) - q_{j+4} - q_{j+1} (j = 1,\ 2) \tag{13}$$

2.2.2. Forward Kinematic

Through the forward kinematic analysis, the position and orientation of the end effector can be calculated from the values of all joints. As shown in Figure 4, three forward kinematic solutions exist as in Equations (14)–(16) because of the characteristics of a parallel mechanism in which three series linkages are constrained to each other.

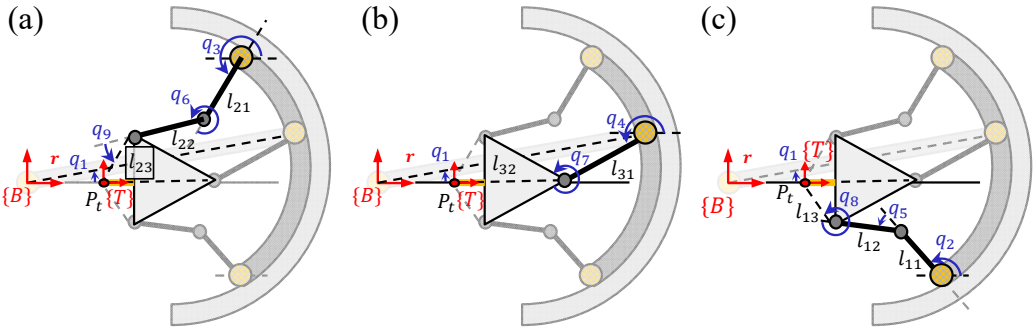

Figure 4. Position of end effector in base coordinate frame according to a serial chain for solving direct kinematic: (**a**) $l_{21} - l_{23}$, (**b**) $l_{31} - l_{32}$, and (**c**) $l_{11} - l_{13}$ serial chains.

$$P_t = \begin{bmatrix} X_t \\ Y_t \\ \theta_t \end{bmatrix} = \begin{bmatrix} r\cos(q_1) + l_{31}\cos(q_4) + l_{32}\cos(q_4 + q_7) \\ r\sin(q_1) + l_{31}\sin(q_4) + l_{32}\sin(q_4 + q_7) \\ q_4 + q_7 + \pi \end{bmatrix} \tag{14}$$

$$P_t = \begin{bmatrix} X_t \\ Y_t \\ \theta_t \end{bmatrix} = \begin{bmatrix} r\cos(q_1 + B) + l_{11}\cos(q_2) + l_{12}\cos(q_2 + q_5) + l_{13}\cos(q_2 + q_5 + q_8) \\ r\sin(q_1 + B) + l_{11}\sin(q_2) + l_{12}\sin(q_2 + q_5) + l_{13}\sin(q_2 + q_5 + q_8) \\ q_2 + q_5 + q_8 + \arccos\left(\frac{l_e}{l_{13}}\right) - \pi \end{bmatrix} \tag{15}$$

$$P_t = \begin{bmatrix} X_t \\ Y_t \\ \theta_t \end{bmatrix} = \begin{bmatrix} r\cos(q_1 + A) + l_{21}\cos(q_3) + l_{22}\cos(q_3 + q_6) + l_{23}\cos(q_3 + q_6 + q_9) \\ r\sin(q_1 + A) + l_{21}\sin(q_3) + l_{22}\sin(q_3 + q_6) + l_{23}\sin(q_3 + q_6 + q_9) \\ q_3 + q_6 + q_9 - \arccos\left(\frac{l_e}{l_{23}}\right) - \pi \end{bmatrix} \tag{16}$$

2.3. Jacobian Analysis

Because the parallel mechanism has a singularity in the workspace, it is necessary to review the singularity and manipulability through a Jacobian analysis. The Jacobian is a type of transformation matrix used for a linear transformation between the joint space representing the velocity of the tool tip. For analysis, all joint vectors $q_i (i = 1\text{–}9)$ are expressed as Equation (17). The relocation matrix U, which divides the dependent and independent joints, and the selection matrix, V, which converts the entire joint vector into an active joint vector, is defined in Equation (18).

$$q_{all} = \begin{bmatrix} q_1 & q_2 & q_3 & q_4 & q_5 & q_6 & q_7 & q_8 & q_9 \end{bmatrix}^T \tag{17}$$

$$q_{all} = U\begin{bmatrix} q_u \\ q_v \end{bmatrix}, \quad q_r = V q_{all} \left(U \in \mathbb{R}^{9\times 9}, V \in \mathbb{R}^{3\times 9}\right) \tag{18}$$

2.3.1. Constrained Jacobian

The constrained Jacobian represents the relationship between the speed of the independent joint and the speed of the dependent joint. As shown in Figure 5, the constraint Jacobian can be obtained through the constraint condition in which the position and posture of the tool tip with respect to the reference coordinate system obtained through each serial chain structure is always constant, which can be expressed through Equation (19).

$$g(q_{all}) = 0 \ : \ \begin{bmatrix} g_1 \\ g_2 \\ g_3 \\ g_4 \\ g_5 \\ g_6 \end{bmatrix} = \begin{bmatrix} x_3 - x_1 \\ y_3 - y_1 \\ \phi_3 - \phi_1 - \tan^{-1}(\frac{t2/2}{l_e}) \\ x_3 - x_2 \\ y_3 - y_2 \\ \phi_3 - \phi_2 + \tan^{-1}(\frac{t2/2}{l_e}) \end{bmatrix} = \begin{bmatrix} 0 \\ 0 \\ 0 \\ 0 \\ 0 \\ 0 \end{bmatrix} \begin{pmatrix} x_i : \ x\ position\ of\ \ chain\ i \\ y_i : \ y\ position\ of\ chain\ i \\ \phi_i : angle\ of\ chain\ i \end{pmatrix} \tag{19}$$

Equation (20) is a process of differentiating the constraint with respect to time, and through this, it is possible to calculate the constraint Jacobian analytically, as in Equation (21). Here, G_u is the Jacobian term for the independent joint vector, and G_v is the Jacobian term for the dependent joint vector.

$$\frac{dg(q_{all})}{dt} = \frac{\partial g(q_{all})}{\partial q_{all}}\frac{dq_{all}}{dt} = G\dot{q}_{all} = 0\ , \left(G \in \mathbb{R}^{6\times 9}\right) \tag{20}$$

$$\begin{bmatrix} G_u & G_v \end{bmatrix}\begin{bmatrix} \dot{q}_u \\ \dot{q}_v \end{bmatrix} = 0 \ \rightarrow \ \dot{q}_v = -G_v^{-1}G_u\dot{q}_u = \Phi\dot{q}_u \tag{21}$$

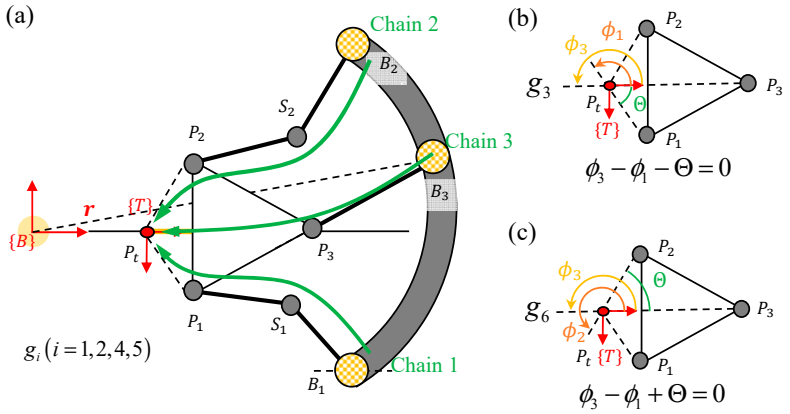

Figure 5. Schematics of six constraint equations considering the posture of the end effector calculated for each serial chain with respect to the base coordinate frame: (**a**) schematics of each serial chain, (**b**) calculated angle of chain 1, (**c**) calculated angle of chain 2.

2.3.2. Forward Jacobian

The forward Jacobian can be obtained through a forward kinematic analysis and constrained Jacobian. From the value of each joint, by differentiating the forward kinematic equations for the position and orientation of the end effector with respect to time, the Jacobian, which represents the speed of all joints with respect to the position and orientation speed of the end effector, can be calculated. By substituting the constrained Jacobian, which represents the relationship between the speed of the independent joint and the speed of the dependent joint, as shown in Equation (22), the relationship between the position and orientation speed of the end effector are represented, and the speed of the independent joint is calculated using Equation (23):

$$\frac{dP_t}{dt} = \frac{\partial P_t}{\partial q_u}\frac{dq_u}{dt} + \frac{\partial P_t}{\partial q_v}\frac{dq_v}{\partial q_u}\frac{dq_u}{dt} = J_u\dot{q}_u + J_v\phi\dot{q}_u, \tag{22}$$

$$\frac{dP_t}{dt} = (J_u + J_v\Phi)\dot{q}_u = J_f\dot{q}_u, \tag{23}$$

where J_u is the Jacobian representing the speed of the position, the orientation of the end effector, and the speed of the independent joint, and J_v is the Jacobian representing the speed of the position, the orientation of the end effector, and the speed of the dependent joint.

3. Workspace Analysis

As described above, the PKM is discontinuous and has a small workspace compared to the size of the mechanism, and thus the design efficiency is low; thus, it does not generally have a workspace suitable for the purpose of the mechanism. Therefore, to increase the design efficiency of the device and secure the desired dexterous workspace for the mechanism, a workspace analysis was conducted, and the kinematic design parameters were optimized.

3.1. Workspace Shape and Condition of Initial Design

The workspace of the proposed parallel kinematic machine has a shape that is rotationally symmetric about the fixed coordinate system centered on the circular guide owing to the hybrid structure. Therefore, the workspace analysis proceeded only in a rectangular area within the range of $0 \leq x \leq 0.3$ [m], $-0.3 \leq y \leq 0.3$ [m] based on the fixed coordinate system, divided the inside into 5 mm intervals, and an inverse kinematic analysis was conducted on all points. In addition, by setting the angular range of the end effector of the mechanism to -35° to 35° and conducting a workspace analysis at intervals of 5°,

the workspace that satisfies all ranges of the end effector in common was defined as the workspace of the mechanism.

To select the initial value of the optimization design parameter, several initial values were defined as summarized in Table 1, and the workspace analysis was conducted and shown in Figure 6. The initial value of 3, which was the largest required workspace, was set as the initial value of the optimization design parameter.

Table 1. Initial value of optimization design parameter.

Design Parameters	L_{11}	L_{12}	L_{21}	L_{22}	L_{31}	A	B
Initial value 1			0.10 m			35°	–35°
Initial value 2			0.11 m				
Initial value 3			0.12 m				
Initial value 4			0.13 m				

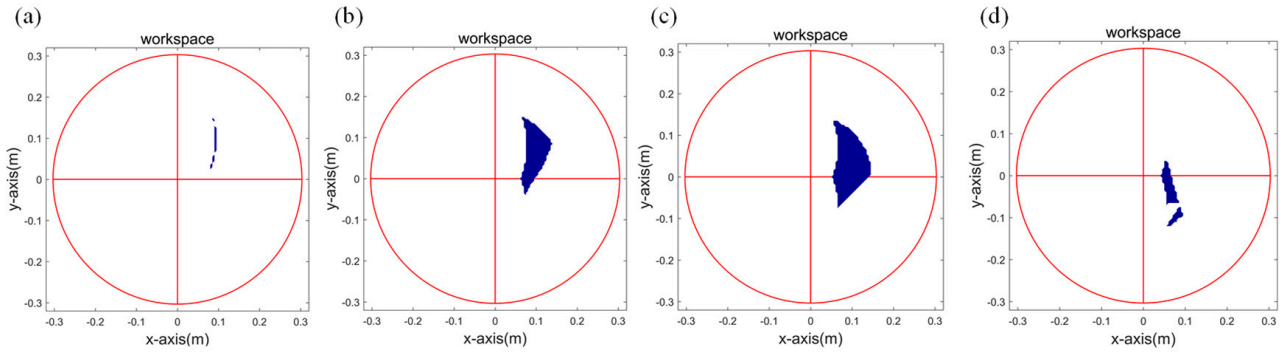

Figure 6. Workspace analysis results according to the initial value of the design parameter: (**a**) initial value 1, (**b**) initial value 2, (**c**) initial value 3, (**d**) initial value 4.

3.2. Workspace Optimization

To overcome the issues related to the workspace and singularity of the PKM and to obtain the optimal workspace for the design purpose, the kinematic parameter was defined as an optimization design parameter, and an optimization based on a genetic algorithm [32] was performed.

3.2.1. Definition of Objective Function

In this study, a weight grid map (WGM) was used to secure an area with a diameter of 200 mm at the center of the circular guide as the optimal workspace for the mechanism. As shown in Figure 7, the WGM is an area where the angle of both sides of the triangle forming the vertex from the center of the circular guide is 60°, and the color of the WGM is a weight that linearly decreases from 1 to zero as it leaves the triangular required workspace. Based on the WGM, the optimization objective function (O.F.) is defined as in Equation (24) such that the design efficiency that minimizes the sum of the linkages of the mechanism while securing the required workspace of the mechanism is maximized. The denominator and numerator of the objective function are normalized to the initial design parameter values to evenly distribute the influence resulting from the unit difference of the design parameters during the optimization process.

$$O.F. = -\log\left(\frac{\left(\sum_{i=1}^{60}\sum_{j=1}^{120} A_{ij} \times w_{ij}\right) / \left(\sum_{i=1}^{60}\sum_{j=1}^{120} A_{ij} \times w_{ij}\right)_{initial}}{(l_{11}+l_{12}+l_{21}+l_{22}+l_{31}) / (l_{11}+l_{12}+l_{21}+l_{22}+l_{31})_{initial}}\right) + \sigma g \quad (24)$$

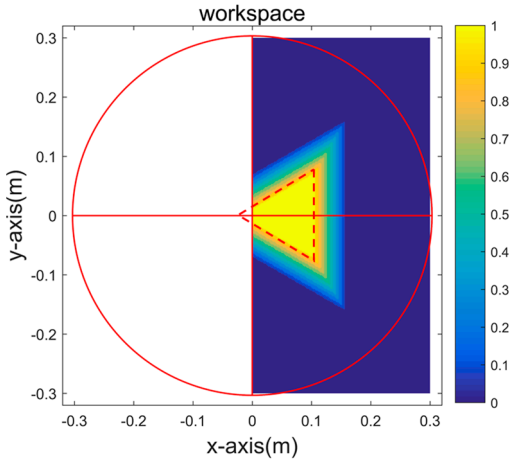

Figure 7. Definition of weighted grid map.

In Equation (24), A_{ij} is the unit area of the workspace grid, which is the i-th in the x-axis and the j-th in the y-axis, w_{ij} is the weight value of the WGM in the grid, and σ and g are the penalty coefficient and penalty condition, respectively.

3.2.2. Optimization Result

Optimization was conducted using the genetic algorithm of the MATLAB optimization toolbox. At this time, since there was a risk of falling into the local optimum if the condition parameter of GA was incorrectly set, it was tuned as shown in Table 2 so that global optimum could be achieved through several trial and errors in advance. In addition, the pseudocode representing the optimization process of the workspace based on the genetic algorithm is shown in Algorithm 1. The optimization results are shown in Table 3, and the workspaces before and after optimization are shown in Figure 8. Through optimization, the area of the optimized workspace within the required workspace of 0.0081 m^2 increased by 81.4% compared to the initial design, and the sum of the optimized link lengths increased by 11.6%, resulting in a 20.4% increase in the design efficiency. As a result, 96.3% of the required workspace, i.e., an area of 0.0078 m^2, could be used as the workspace of the mechanism.

Algorithm 1. Optimization algorithm based on genetic algorithm

While function value
Do {
1. Set the design parameters and position of the end effector
for orientation of the end-effector(θ_t) = $-10{:}1{:}10$
(1) Calculate the workspace by weighted grid
(2) Sum the length of links
$(l_{11} + l_{12} + l_{21} + l_{22} + l_{31})$
(3) Calculate the value of objective function
end
2. Find the minimum value of objective function
}

Table 2. Condition of genetic algorithm for optimization.

Number of Variables	7(L_{11}, L_{12}, L_{21}, L_{22}, L_{31}, A, B)
Lower bound	0.04 0.04 0.04 0.04 0.04 20 −20]
Upper bound	[0.24 0.24 0.24 0.24 0.24 60 −60]
Population type	Double vector
Population size	200
Creation function	Constraint dependent
Fitness scaling	Proportional
Selection	Uniform
Mutation	Adaptive feasible
Crossover	Scattered
Stopping criteria	Function tolerance: 1×10^{-4}

Table 3. Optimization results: value of design parameter, required workspace, sum of link length.

Design Parameters	l_{11}**[m]**	l_{12}**[m]**	l_{21}**[m]**	l_{22}**[m]**	l_{31}**[m]**	A **[°]**	B **[°]**
Initial variables	0.15	0.15	0.15	0.15	0.15	40	−40
Optimized variables	0.1092	0.1431	0.0697	0.1995	0.1624	29.49	−38.26

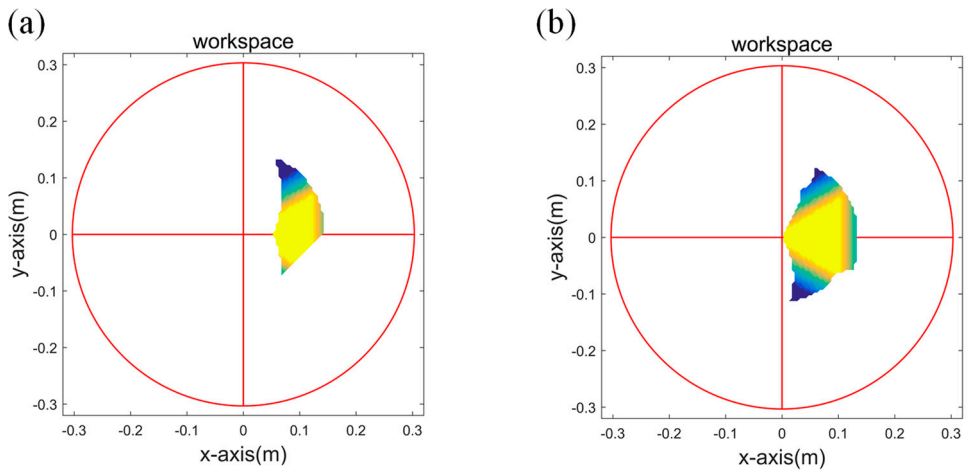

Figure 8. Workspace plot of proposed 3-DOF planar PKM: workspace for (**a**) initial design parameters and (**b**) optimized design parameters.

3.3. Singularity Analysis

A singularity analysis was conducted to remove the uncontrollable area within the workspace of the PKM. For a singularity analysis, the isotropy and manipulability, which are quantified singularity evaluation indicators, were defined, and a singularity analysis according to the active joint combination for the optimized workspace obtained in the previous section was conducted in the case of 1-DOF redundant actuation and nonredundant actuation.

3.3.1. Isotropy and Manipulability

In many studies, evaluation of the singularity area within the workspace of the PKM has been generally conducted using the eigenvalue. In this study, as in the above studies, a singularity point analysis was applied using the eigenvalue and eigenvector of the forward

Jacobian matrix, and the eigenvalues and eigenvectors of the forward Jacobian matrix were calculated through the eigenvalue decomposition, as shown in Equation (25).

$$J_f = U\Sigma V^T,\ \Sigma = \begin{bmatrix} \sigma_1 & & \cdots & 0 & 0 \\ & \sigma_2 & & & 0 \\ \vdots & & \ddots & \vdots & \\ 0 & & \cdots & \sigma_n & 0 \end{bmatrix} (n : DOF\ of\ PKM) \tag{25}$$

where the matrices U and V are the left and right eigenvectors, respectively, and matrix $\sum$ is an eigenvalue matrix in the form of a diagonal matrix. The isotropy of the velocity(s) at a point in the workspace is defined as the condition number of the forward Jacobian, as in Equation (26), and the manipulability is defined as the product of all eigenvalues of the forward Jacobian matrix, as in Equation (27).

$$s = \frac{1}{\kappa} = \frac{\lambda_{\min}}{\lambda_{\max}},\ 0 \le s \le 1 \tag{26}$$

$$w = \sqrt{\det J_f J_f^T} = \lambda_1 \lambda_2 \cdots \lambda_n\ (n : dimension) \tag{27}$$

Figure 9 shows an example of the singularity analysis of the case in which the mechanism does and does not have a singularity. The velocity ellipsoid attached to the end effector is a tool for visualizing the isotropy and manipulability. The isotropy is defined as the ratio of the size of the major axis to the minor axis of the velocity ellipsoid and is the ratio of the maximum and minimum velocities that can be instantaneously moved at a point in the workspace. By contrast, the manipulability is defined as the product of the magnitudes of all axes of the velocity ellipsoid and is the product of all velocities at a point in the workspace.

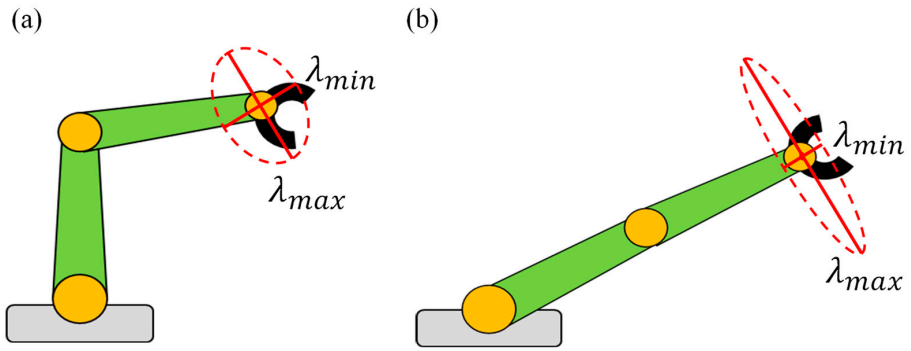

Figure 9. Example of singularity analysis: (**a**) singularity and (**b**) nonsingularity shapes.

3.3.2. Analysis Results According to the Combination of Active Joints

The active joint combination considers six combinations of nonredundant cases, as shown in Table 4. The singularity analysis was conducted through the isotropy and manipulability analysis of these six combinations, and 1-DOF redundancy was considered for the combination with the best singularity area removal performance.

Table 4. Set of active joint.

Set 1	Configuration	Set 2	Configuration
Combination between joints on arc-shaped frame	$q_1 - q_2 - q_3$ $q_1 - q_2 - q_4$ $q_1 - q_3 - q_4$	Combination according to the serial chain structure	$q_1 - q_2 - q_5$ $q_1 - q_3 - q_6$ $q_1 - q_4 - q_7$

Table 5 shows the mean and standard deviation of isotropy and manipulability for the singularity analysis results. A singularity analysis was conducted for -30°, 0°, and 30° of the end effector angles, and the results are shown in Appendix A. The average isotropy increased from a minimum of 1.098×10^3% to a maximum of 1.275×10^3% through 1-DOF redundancy, and the standard deviation of manipulability was highly reduced. This means that the size ratio of the minor axis and the major axis of the velocity ellipsoid in the singularity area decreased, and the manipulability for the minor axis direction in which the mechanism cannot move instantaneously increased. As a result, it was possible to remove the singularity area through 1-DOF redundancy.

Table 5. Analysis result of isotropy and manipulability: average and deviation.

Actuate Set		**Nonredundant**		**Redundant**	
		$q_1 - q_2 - q_4$		$q_1 - q_2 - q_4 - q_7$	
Index		**Isotropy**	**Manipulability**	**Isotropy**	**Manipulability**
Angle of end effector	–30°	0.0045 ± 0.0024	0.7473 ± 4.1905	0.0619 ± 0.0080	0.0446 ± 0.0081
	0°	0.0050 ± 0.0028	1.7840 ± 35.6422	0.0632 ± 0.0062	0.0475 ± 0.0069
	30°	0.0053 ± 0.0034	0.9262 ± 5.4762	0.0635 ± 0.0066	0.0474 ± 0.0081

4. Kinematic Stiffness Analysis

For the cases of nonredundancy and 1-DOF redundancy, the distribution of the displacement of the end effector over the entire workspace was analyzed. Therefore, the mechanism stiffness model of the end effector for a given cutting reaction was defined for the nonredundant case and the 1-DOF redundant case to analyze the difference between them.

The mechanism stiffness was divided into structural stiffness and kinematic stiffness, of which the latter was obtained by the sum of the active stiffness determined by the active joint combination and passive stiffness determined by the rotational stiffness of the active joint. Unlike structural stiffness, which considers the deformation of the mechanical parts by external force, kinematic stiffness is calculated by assuming that the parts are rigid bodies. Because the link part of the PKM has a much higher stiffness than the joint part, this study assumed that the link part is a rigid body and only considered this kinematic stiffness.

4.1. Kinematic Stiffness Modeling for Nonredundant Case

As described above, the kinematic stiffness is classified into passive and active stiffness depending on whether control through redundancy is possible. Because passive stiffness is determined by the rotational stiffness of the drive motor and the shape of the mechanism, control through redundancy is impossible, but active stiffness can be adjusted through torque control of the drive motor. Before the kinematic stiffness analysis, the virtual work theory was applied through Equation (28) below to express the relationship between the force applied on the end effector in the Cartesian coordinate space and the torque of the driving joint in the joint space.

$$\tau^T dq_r + F^T dx = 0 \tag{28}$$

The left term refers to the work caused by the driving joint, and the rightmost term refers to the work owing to the external force applied to the end effector. In the case of nonredundancy, because the driving joint is the same as the independent joint, τ^T and dq_r denote the 3×1 driving torque vector in the joint space and the 3×1 micro displacement vector of the driving joint, respectively, and the microdisplacement vector of the driving joint can be expressed as Equation (29) through the forward Jacobian. Equation (30) summarizes this for the external forces.

$$\tau^T (J_f^{-1}) dx + F^T dx = 0 \tag{29}$$

$$F = (J_f^{-1})^T(-\tau) \tag{30}$$

Because stiffness is the magnitude of the external force for unit deformation, Equation (30) can be differentiated with respect to the spatial displacement and expressed as the stiffness of the end effector of the mechanism, as shown in Equation (31) below. As shown in Equation (32), it can be divided into two terms by expanding it through a chain rule:

$$K = \frac{df}{dx} = \frac{d(J_f^{-1})^T(-\tau)}{dx} \tag{31}$$

$$K = \frac{d(J_f^{-1})^T}{dx} \otimes (-\tau) + (J_f^{-1})^T \frac{d(-\tau)}{dx} \tag{32}$$

The driving torque can be expressed as Equation (33) below as a vector of the rotational stiffness of the driving motor and a small displacement of the driving joint. The rotational stiffness of the drive motor is a 3×3 diagonal matrix, and the diagonal matrix element represents the rotational stiffness of each drive motor. Substituting this equation into Equation (32), the result can be expressed as Equation (34):

$$\tau = K_\tau dq_\tau \tag{33}$$

$$K = \frac{d(J_f^{-1})^T}{dq_u} J_f^{-1} \otimes (-\tau) + (J_f^{-1})^T K_\tau J_f^{-1} \tag{34}$$

In Equation (34), the left term is the active stiffness, and the right term is the passive stiffness. In the case of nonredundancy, the active stiffness and passive stiffness are dependent on the forward Jacobian, and thus it becomes a function of the shape of the mechanism and cannot be controlled by the drive motor.

4.2. Kinematic Stiffness Modeling for 1-DOF Redundancy Case

In 1-DOF redundancy, the driving joint vector includes not only the independent joint vector but also the dependent joint vector. To express the relationship between the driving joint vector and the independent joint vector, a new Jacobian Γ is defined as Equation (35) below:

$$\Gamma = VU \begin{bmatrix} I_3 \\ \Phi \end{bmatrix} \tag{35}$$

In the case of 1-DOF redundancy, Equation (28) is used to obtain the kinematic stiffness, as with nonredundancy. In addition, τ^T and dq_r denote the 4×1 driving torque vector and the 4×1 microdisplacement vector of the drive joint in the joint space, respectively, and the microdisplacement vector of the drive joint can be expressed as Equation (36) below through Γ.

$$\tau^T \Gamma (J_f^{-1}) dx + F^T dx = 0 \tag{36}$$

After summarizing this for the external force, the stiffness for the end effector can be obtained as Equation (37) by differentiating it for the displacement in the Cartesian coordinate space. The term multiplied by the Jacobian Γ and the forward Jacobian's inverse matrix can be expressed simply as Equation (38) by defining a 4×3 Jacobian ψ, which is the relationship between the driving joint and the displacement of the Cartesian coordinate space, and can be expressed as Equation (39) by developing the derivative using a chain rule.

$$K = \frac{df}{dx} = \frac{d(\Gamma(J_f^{-1}))^T(-\tau)}{dx} \tag{37}$$

$$K = \frac{df}{dx} = \frac{d(\psi)^T(-\tau)}{dx} \tag{38}$$

$$K = \frac{d(\psi)^T(-\tau)}{dx} = \frac{d(\psi)^T}{dx} \otimes (-\tau) + (\psi)^T \frac{d(-\tau)}{dx} \tag{39}$$

As described above, the driving torque is the same as the rotational stiffness of the driving motor and the microdisplacement vector of the driving joint as in Equation (33), and the rotational stiffness of the driving motor is a 4×4 diagonal matrix that is different from the nonredundancy case. Therefore, by substituting this into Equation (39), it can be expressed in terms of active and passive stiffness, as in Equation (40). The Jacobian ψ, which represents the displacement relationship between the driving joint and the Cartesian coordinate space, is dependent on the shape of the mechanism. The rotational stiffness matrix K_r of the drive motor is determined by the characteristics of the motor, and thus the passive stiffness term is independent of the displacement of the Cartesian coordinates. By contrast, in the active stiffness term, Jacobian ψ is differentiated with respect to the driving joint such that the value of the active stiffness changes according to the minute displacement of the driving joint. In this study, the active stiffness was calculated using the least-squares method.

$$K = \frac{d(\psi)^T}{dq_r}\psi \otimes (-\tau) + (\psi)^T K_r \psi \tag{40}$$

4.3. Displacement Analysis

The amount of displacement for kinematic stiffness for the entire workspace was analyzed by dividing into a case of nonredundancy and 1-DOF redundancy and analyzing the isotropy and magnitude of the stiffness matrix. The isotropy and magnitude analysis of the stiffness matrix was conducted by analyzing the eigenvalues and eigenvectors of the stiffness matrix using the same method as described in the singularity analysis. The reaction force considered in the displacement analysis was set to 7N by applying a safety factor of 2 to the cutting reaction force [28] for the 0.5 mm cutting depth of the PLA material, which is an industrial plastic. In addition, the rotation direction displacement was not considered owing to the characteristics of the cutting tool composed of a ball end mill, and the driving joint set applied to the simulation was $q_2 - q_3$ for the nonredundancy and $q_2 - q_3 - q_4$ for the 1-DOF redundancy. The results of the analysis of stiffness and displacement according to the angle of the end effector are shown in Appendix B, and the results of the displacement amount, isotropy, and magnitude of the stiffness as well as a torque analysis are shown in Table 6.

Table 6. Analysis results: displacement amount, magnitude, and isotropy of stiffness, along with the maximum and minimum of torque.

Tool Angle	Driving Method	Stiffness		Displacement Amount [μm]	Torque Norm [Nm]	Actuator Torque [Nm]			Torque Norm at Global Maxima [Nm]
		Magnitude	Isotropy			q_2	q_3	q_4	
−30°	Nonredundant	2.76×10^{10}	5.50×10^{-2}	78.0	1.169	−1.090	−0.421	-	1.169
	1-redundant	4.21×10^{10}	3.13×10^{-2}	46.1	0.920	−0.562	−0.552	0.474	0.926
0°	Nonredundant	3.17×10^{10}	6.86×10^{-2}	70.9	1.037	−0.959	−0.393	-	1.037
	1-redundant	5.32×10^{10}	5.86×10^{-2}	40.2	0.822	−0.477	−0.556	−0.373	0.834
30°	Nonredundant	3.20×10^{10}	4.72×10^{-4}	101.9	1.289	−1.280	0.128	-	1.289
	1-redundant	5.97×10^{10}	4.14×10^{-4}	33.2	0.739	−0.473	−0.472	−0.316	0.739

From the results shown in Appendix B, it can be seen that the size of the minor axis and the major axis of the velocity ellipsoid increased through 1-DOF redundancy, but it is difficult to confirm the decrease in the ratio. In other words, it can be seen that the

magnitude of the stiffness generally improved through 1-DOF redundancy, but the stiffness isotropy meant there was no significant change.

As shown in Table 6, the displacement amount decreased by 40.9%, 43.3%, and 67.4%, respectively, and the required torque decreased by 21.3%, 20.7%, and 42.7%, through 1-DOF redundant compared to nonredundant within the required work area. As a result, it can be confirmed theoretically that the magnitude of the stiffness is improved and the amount of displacement at the end effector is reduced through 1-DOF redundancy.

5. Conclusions

In this study, the optimal design of a cutting stage based on 3-DOF redundant PKM for improving the surface roughness of FDM-type sculptures was examined. While the proposed cutting stage satisfied the required workspace of a triangular shape with an area of 0.0081 m^2, the design efficiency including a WGM was presented as an objective function to minimize the size of the PKM, and the optimization of the workspace based on the genetic algorithm was performed. As a result, the efficiency of the optimal design increased by 20.4% compared to the initial design, and an optimal design was derived with an area of 0.0078 m^2, which was 96.3% of the required workspace, as the workspace of the PKM.

In addition, velocity isotropy and manipulability were applied as evaluation indices to analyze the area singularity existing in the optimized workspace. A singularity analysis was conducted according to the driving joint, and the optimal combination of driving joints based on 1-DOF redundancy that maximizes the velocity isotropy and manipulability while removing the singularity was derived.

Finally, based on the virtual work theory, a kinematic stiffness model was established for the external force applied to the end effector. The cutting reaction force against the PLA material was applied as an external force, and the displacement characteristics at the end effector were examined for each case of 1-DOF redundancy and nonredundancy. As a result, the amount of displacement decreased by 40.9%, 43.3%, and 67.4%, respectively, through 1-DOF redundancy.

Future research on this topic should focus on actually fabricating and experimenting with PKM with optimized parameters. The vibration characteristics at the singular point in the workspace of the cutting part PKM end effector can be checked and compared with the simulation result, and based on this, it is possible to check whether there is room for improvement for the development of the next version in the future.

Author Contributions: Conceptualization, D.L. and M.L.; investigation, M.L. and H.J.; validation, D.L. and M.L.; supervision, D.L.; writing, H.J. and D.L. All authors have read and agreed to the published version of the manuscript.

Funding: This work was supported by the Basic Science Research Program through a National Research Foundation of Korea (NRF) grant funded by the Ministry of Education (NRF-2016R1D1A1B03932054) and the Korean government (MSIT) (NRF-2019R1F1A1045834).

Institutional Review Board Statement: Not applicable.

Informed Consent Statement: Not applicable.

Data Availability Statement: Not applicable.

Conflicts of Interest: The authors declare no conflict of interest.

Appendix A

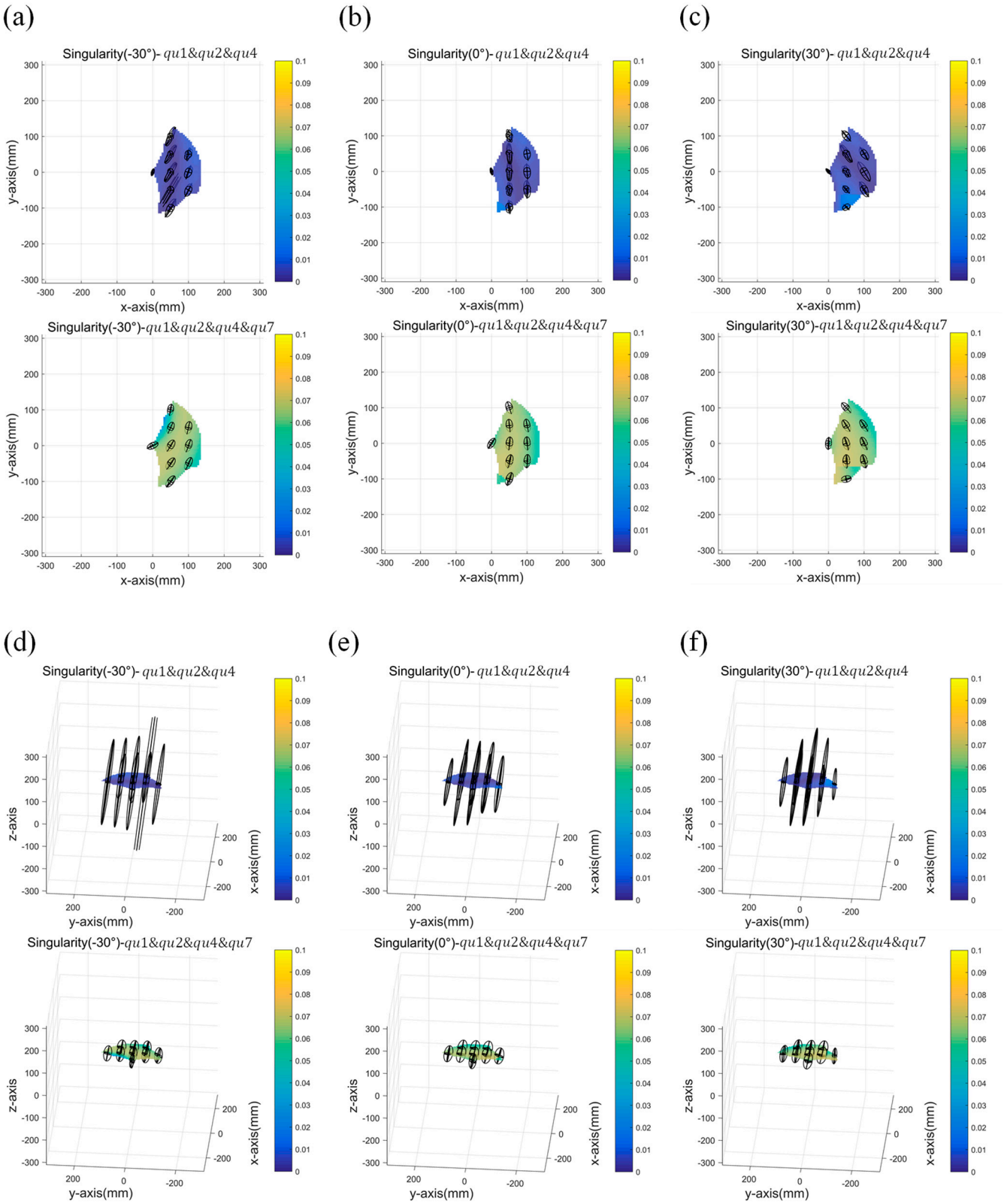

Figure A1. Singular point analysis results according to the angle of the end effector (upper figure is nonredundant, lower figure is 1-redundant): (**a**–**c**) are top view, and (**d**–**f**) are side view.

Appendix B

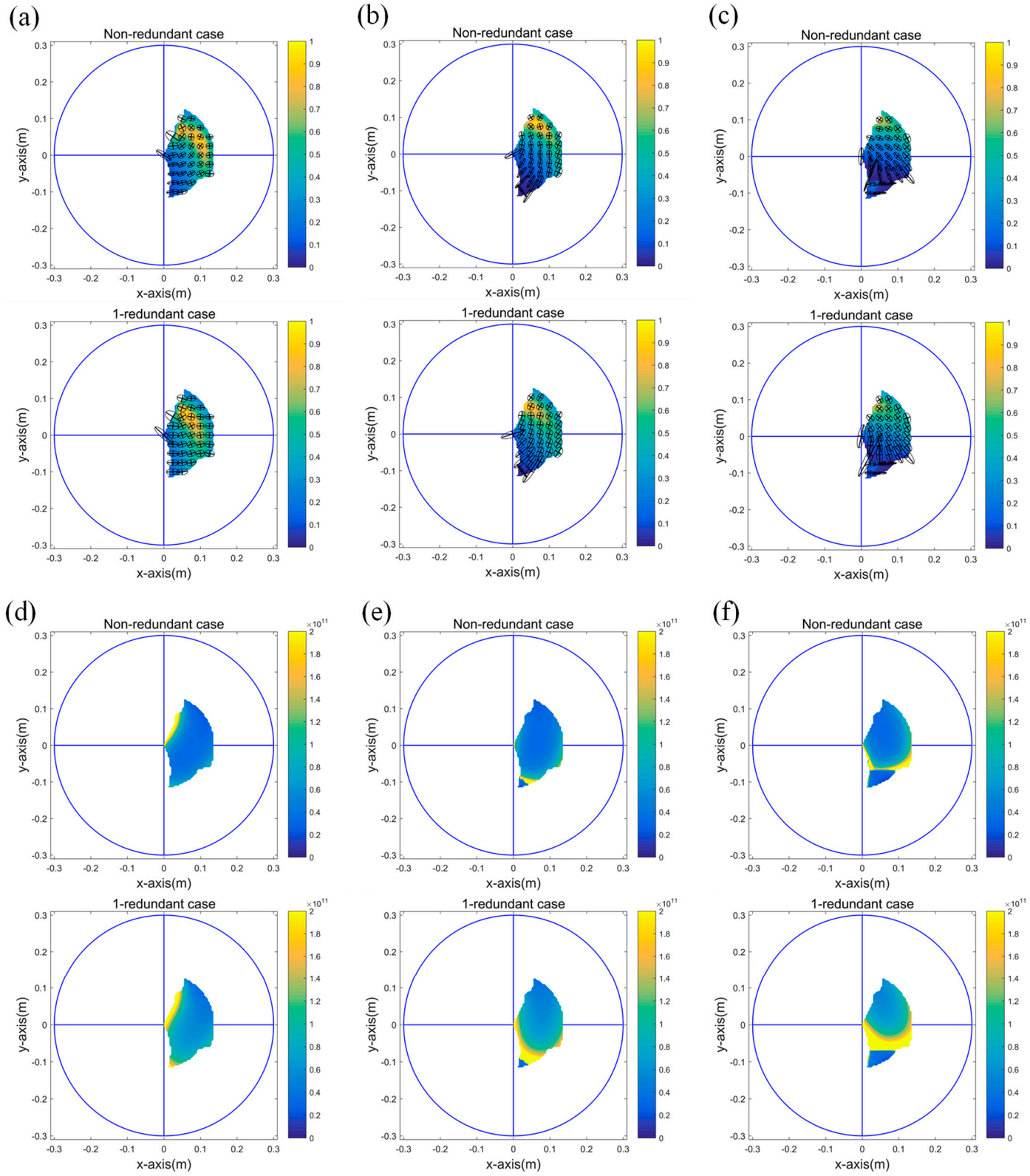

Figure A2. *Cont*.

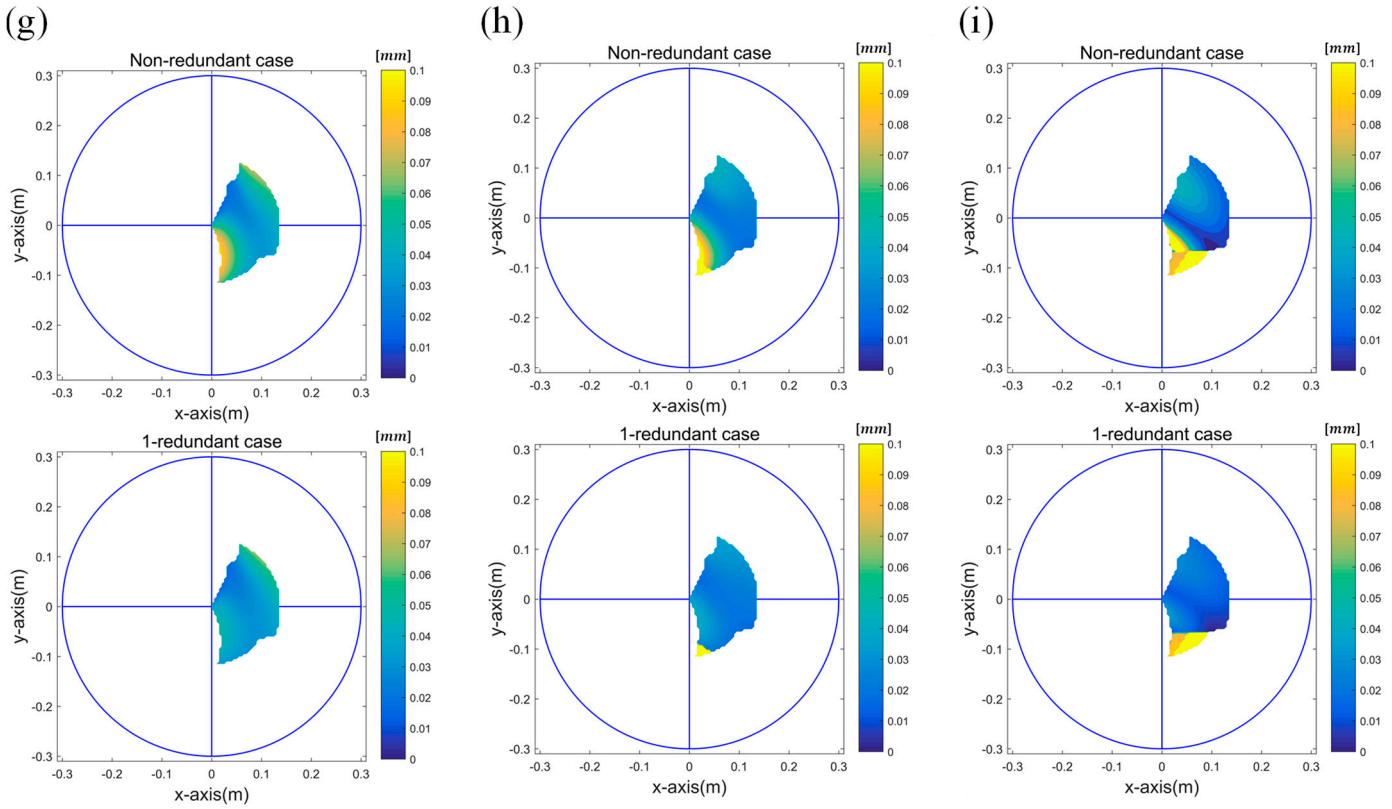

Figure A2. Stiffness analysis result according to the angle of the end effector. (**a**–**c**) results of stiffness isotropic analysis at −30°, 0°, and 30°; (**d**–**f**) results of stiffness magnitude analysis at −30°, 0°, and 30°; (**g**–**i**) results of displacement amount analysis at −30°, 0°, and 30°.

References

1. Aslani, K.-E.; Chaidas, D.; Kechagias, J.; Kyratsis, P.; Salonitis, K. Quality Performance Evaluation of Thin Walled PLA 3D Printed Parts Using the Taguchi Method and Grey Relational Analysis. *J. Manuf. Mater. Process.* **2020**, *4*, 47. [CrossRef]
2. Aslani, K.E.; Kitsakis, K.; Kechagias, J.D.; Vaxevanidis, N.M.; Manolakos, D.E. On the application of grey Taguchi method for benchmarking the dimensional accuracy of the PLA fused filament fabrication process. *SN Appl. Sci.* **2020**, *2*, 1016. [CrossRef]
3. Chen, S.L.; Chang, T.H.; Inasaki, I.; Liu, Y.-C. Post-Processor Development of a Hybrid TRR-XY Parallel Kinematic Machine Tool. *Int. J. Adv. Manuf. Technol.* **2002**, *20*, 259–269. [CrossRef]
4. Liang, Q.; Zhang, D.; Coppola, G.; Mao, J.; Sun, W.; Wang, Y.; Ge, Y. Design and Analysis of a Sensor System for Cutting Force Measurement in Machining Processes. *Sensors* **2016**, *16*, 70. [CrossRef] [PubMed]
5. Jeong, H.; Yu, J.; Lee, D. Calibration of In-Plane Center Alignment Errors in the Installation of a Circular Slide with Machine-Vision Sensor and a Reflective Marker. *Sensors* **2020**, *20*, 5916. [CrossRef]
6. Pateloup, S.; Chanal, H.; Duc, E. Geometric and Kinematic Modelling of a New Parallel Kinematic Machine Tool: The Tripteor X7 Designed by PCI. *Adv. Mater. Res.* **2010**, *112*, 159–169. [CrossRef]
7. Gao, F.; Liu, X.J.; Chen, X. The relationships between the shapes of the workspaces and the link lengths of 3-DOF symmetrical planar parallel manipulators. *Mech. Mach. Theory* **2001**, *36*, 205–220. [CrossRef]
8. Glozman, D.; Shoham, M. Novel 6-DOF parallel manipulator with large workspace. *Robotica* **2009**, *27*, 891–895. [CrossRef]
9. Li, H.; Gosselin, C.M.; Richard, M.J. Determination of maximal singularity-free zones in the workspace of planar three-degree-of-freedom parallel mechanisms. *Mech. Mach. Theory* **2006**, *41*, 1157–1167. [CrossRef]
10. Masouleh, M.T.; Gosselin, C. Determination of singularity-free zones in the workspace of planar 3-PRR parallel mechanisms. *J. Mech. Des.* **2007**, *129*, 649–652. [CrossRef]
11. Abbasnejad, G.; Daniali, H.M.; Kazemi, S.M. A new approach to determine the maximal singularity-free zone of 3-RPR planar parallel manipulator. *Robotica* **2012**, *30*, 1005–1012. [CrossRef]
12. Cha, S.H.; Lasky, T.A.; Velinsky, S.A. Singularity avoidance for the 3-RRR mechanism using kinematic redundancy. In Proceedings of the 2007 IEEE International Conference on Robotics and Automation, Rome, Italy, 10–14 April 2007.
13. Kotlarski, J.; Abdellatif, H.; Ortmaier, T.; Heimann, B. Enlarging the useable workspace of planar parallel robots using mechanisms of variable geometry. In Proceedings of the 2009 ASME/IFToMM International Conference on Reconfigurable Mechanisms and Robots, London, UK, 22–24 June 2009.

14. Wang, G.; Wang, Y.; Zhao, J.; Chen, G. Process optimization of the serial-parallel hybrid polishing machine tool based on artificial neural network and genetic algorithm. *J. Intell. Manuf.* **2012**, *23*, 365–374. [CrossRef]
15. Wang, M.; Liu, H.; Huang, T.; Chetwynd, D.G. Compliance analysis of a 3-SPR parallel mechanism with consideration of gravity. *Mech. Mach. Theory* **2015**, *84*, 99–112. [CrossRef]
16. Yang, X.; Zhao, J.; Zhang, L.; Li, D.; Li, R. A novel surface self-adapting parallel machine tool for blade machining. In Proceedings of the 2009 International Conference on Mechatronics and Automation, Changchun, China, 9–12 August 2009.
17. Zhang, H.; Fang, H.; Fang, Y.; Jiang, B. Workspace analysis of a hybrid kinematic machine tool with high rotational applications. *Math. Probl. Eng.* **2018**, *2018*, 2607497. [CrossRef]
18. Kanaan, D.; Wenger, P.; Chablat, D. Kinematic analysis of a serial–parallel machine tool: The VERNE machine. *Mech. Mach. Theory* **2009**, *44*, 487–498. [CrossRef]
19. Wu, J.; Wang, J.; Wang, L.; Li, T.; You, Z. Study on the stiffness of a 5-DOF hybrid machine tool with actuation redundancy. *Mech. Mach. Theory* **2009**, *44*, 289–305. [CrossRef]
20. Xu, P.; Cheung, C.-F.; Li, B.; Ho, L.-T.; Zhang, J.-F. Kinematics analysis of a hybrid manipulator for computer controlled ultra-precision freeform polishing. *Rob. Coput. Integr. Manuf.* **2017**, *44*, 44–56. [CrossRef]
21. Wang, Z.; Ji, S.; Sun, J.; Wan, Y.; Yuan, Q.; Zheng, L. A methodology for determining the maximal regular-shaped dexterous workspace of the PMs. In Proceedings of the 2007 International Conference on Mechatronics and Automation, Harbin, China, 5–8 August 2007.
22. Lee, D.H.; Kim, J.W.; Seo, T.W. Optimal design of 6-DOF eclipse mechanism based on task-oriented workspace. *Robotica* **2012**, *30*, 1041–1048. [CrossRef]
23. Liu, X.J.; Wang, J.; Oh, K.K.; Kim, J. A taking the approach to the design of a DELTA robot with a desired workspace. *J. Intell. Rob. Syst.* **2004**, *39*, 209–225. [CrossRef]
24. Lou, Y.; Liu, G.; Chen, N.; Li, Z. Optimal design of parallel manipulators for maximum effective regular workspace. In Proceedings of the 2005 IEEE/RSJ International Conference on Intelligent Robots and Systems; Institute of Electrical and Electronics Engineers (IEEE), Edmonton, AB, Canada, 2–6 August 2005.
25. Saglia, J.A.; Dai, J.S.; Caldwell, D.G. Geometry and kinematic analysis of a redundantly actuated parallel mechanism that eliminates singularities and improves dexterity. *J. Mech. Des.* **2008**, *130*, 124501. [CrossRef]
26. Saafi, H.; Laribi, M.A.; Zeghloul, S. Redundantly actuated 3-RRR spherical parallel manipulator used as a haptic device: Improving dexterity and eliminating singularity. *Robotica* **2015**, *33*, 1113–1130. [CrossRef]
27. Huang, T.; Li, M.; Li, Z.; Chetwynd, D.; Whitehouse, D. Optimal kinematic design of 2-DOF parallel manipulators with well-shaped workspace bounded by a specified conditioning index. *IEEE Trans. Robot. Autom.* **2004**, *20*, 538–543. [CrossRef]
28. Lara-Molina, F.A.; Rosario, J.M.; Dumur, D. Multi-objective design of parallel manipulator using global indices. *Open Mech. Eng. J.* **2010**, *4*, 37–47. [CrossRef]
29. Huang, M.Z.; Thebert, J.L. A study of workspace and singularity characteristics for design of 3-DOF planar parallel robots. *Int. J. Adv. Manuf. Technol.* **2010**, *51*, 789–797. [CrossRef]
30. Huang, T.; Li, M.; Zhao, X.M.; Mei, J.P.; Chetwynd, D.G.; Hu, S.J. Conceptual design and dimensional synthesis for a 3-DOF module of the TriVariant-a novel 5-DOF reconfigurable hybrid robot. *IEEE Trans. Robot.* **2005**, *21*, 449–456. [CrossRef]
31. Laribi, M.A.; Romdhane, L.; Zeghloul, S. Analysis and dimensional synthesis of the DELTA robot for a prescribed workspace. *Mech. Mach. Theory* **2007**, *42*, 859–870. [CrossRef]
32. Yu, Y.; Li, J.; Li, Y.; Li, S.; Li, H.; Wang, W. Comparative Investigation of Phenomenological Modeling for Hysteresis Responses of Magnetorheological Elastomer Devices. *Int. J. Mol. Sci.* **2019**, *20*, 3216. [CrossRef] [PubMed]